LETTER

Observation of the frozen charge of a Kondo resonance

M. M. Desjardins[1], J. J. Viennot[2], M. C. Dartiailh[1], L. E. Bruhat[1], M. R. Delbecq[3]†, M. Lee[4], M.-S. Choi[5], A. Cottet[1] & T. Kontos[1]

The ability to control electronic states at the nanoscale has contributed to our modern understanding of condensed matter. In particular, quantum dot circuits represent model systems for the study of strong electronic correlations, epitomized by the Kondo effect[1–3]. We use circuit quantum electrodynamics architectures to study the internal degrees of freedom of this many-body phenomenon. Specifically, we couple a quantum dot to a high-quality-factor microwave cavity to measure with exceptional sensitivity the dot's electronic compressibility, that is, its ability to accommodate charges. Because electronic compressibility corresponds solely to the charge response of the electronic system, it is not equivalent to the conductance, which generally involves other degrees of freedom such as spin. Here, by performing dual conductance and compressibility measurements in the Kondo regime, we uncover directly the charge dynamics of this peculiar mechanism of electron transfer. The Kondo resonance, visible in transport measurements, is found to be 'transparent' to microwave photons trapped in the high-quality cavity, thereby revealing that (in such a many-body resonance) finite conduction is achieved from a charge frozen by Coulomb interaction. This freezing of charge dynamics[4–6] is in contrast to the physics of a free electron gas. We anticipate that the tools of cavity quantum electrodynamics could be used in other types of mesoscopic circuits with many-body correlations[7,8], providing a model system in which to perform quantum simulation of fermion–boson problems.

In a free electron gas, electrical conduction is due to mobile charges. Its compressibility, $\chi = \frac{\partial N}{\partial \mu}$ with N the number of electrons and μ the chemical potential, is simply the density of states at the Fermi energy, and is therefore directly linked to the finite conductivity of the system. This explains why, for example, both the compressibility and the conductivity provide essentially the same piece of information for alkali metals. But what happens in the case of a strongly correlated electron gas? A prominent paradigm is that of an electron localized on a single site with strong Coulomb repulsion, coupled to a continuum of electronic states[1–4,7–9]. Through its link to the Kondo problem, such a configuration, besides its apparent simplicity, is relevant for understanding different types of strongly correlated gases—ranging from heavy fermions to high-T_c superconductors[4,9]—and therefore a priori relevant for many condensed matter problems.

A single localized level is expected to have a much smaller electronic compressibility than a piece of metal, because its density of states at the Fermi energy is dramatically reduced. We now consider how to measure the tiny compressibility of a single localized state. Such a measurement first requires a single electron to be isolated in a controlled manner. This can be conveniently done using a quantum dot (QD) circuit, but we also need to measure its tiny effective capacitance, which is equivalent to the compressibility of an electron gas. Although this can be done using low-frequency as well as microwave techniques[10–13], it

has been shown recently that this could be achieved alternatively with an unprecedented sensitivity using a circuit quantum electrodynamics architecture[14]. We note that correlation effects have been sought since the first compressibility measurements in quantum dots[10]. Our work is, to our knowledge, the first in which correlation effects are directly (and qualitatively) visible in the compressibility of a quantum dot circuit[5,6]. To achieve this visibility, we use the prototype example of the Kondo regime.

The principle of our measurement architecture is shown in Fig. 1a: the finite compressibility χ shifts the frequency of the microwave resonator (as shown in Fig. 1b), which is used here as a non-invasive probe (see Methods). This frequency shift, read out from the phase of the microwave signal, is only sensitive to variations of the dot charge, in contrast to the conductance for which all degrees of freedom can contribute (charge and spin). The linewidth of the cavity and the strength of the electron–photon coupling set the limit to the smallest detectable χ.

The experimental set-up is shown in Fig. 1c. A single quantum dot circuit made out of a single-wall carbon nanotube is embedded in a coplanar waveguide cavity and coupled capacitively[15] to it (see Methods). We measure simultaneously the DC current flowing through the quantum dot and the phase and amplitude of the transmitted microwave signal at the cavity frequency ($f_{cav} = 6.67129$ GHz). Such a set-up allows us to characterize the electron–photon interaction accurately, which is essential for performing a compressibility measurement.

Carbon nanotube QDs can be tuned from the deep Coulomb blockade regime to the Kondo regime[16] simply by changing the voltage V_g applied to an electrostatic gate (coloured green in Fig. 1c). For low gate voltages, we observe standard Coulomb diamonds in the V_g–V_{sd} plane, where V_{sd} is the source–drain bias. Figure 2a and b displays the characteristic periodic patterns of the conductance and the microwave phase in this regime at the base temperature of our experiment, $T = 255$ mK. The conductance resonances delimiting the Coulomb diamonds appear simultaneously as peaks of about 3° in the phase signal. This indicates a finite compressibility of the QD electron gas for these resonances. In contrast, in a Coulomb valley, the charge dynamics in the dot is frozen, which leads to the absence of compressibility, as shown in Fig. 2d. The finite compressibility and the peaks in the conductance are perfectly correlated (see Fig. 2c), which is reminiscent of a weakly correlated electron gas although interactions are present, manifested by Coulomb blockade.

The nature and the strength of the electron–photon coupling in our device is calibrated using a well-known phenomenon, namely Coulomb blockade in the linear regime (bias $eV_{sd} < k_B T$, Fig. 2c). In that case, electron transport only occurs when the electron gas in the QD has a finite density of states at the Fermi energy, which also corresponds to a finite compressibility[17–19]. Because the finite compressibility is linked to back and forth tunnelling of electrons between the QD and the leads, it creates a dipole which couples to the cavity (see Fig. 2e, top panel).

[1]Laboratoire Pierre Aigrain, Ecole Normale Supérieure-PSL Research University, CNRS, Université Pierre et Marie Curie-Sorbonne Universités, Université Paris Diderot-Sorbonne Paris Cité, 24 rue Lhomond, 75231 Paris Cedex 05, France. [2]JILA and Department of Physics, University of Colorado, Boulder, Colorado 80309, USA. [3]Center for Emergent Matter Science, RIKEN, 147 Main Building, 2-1 Hirosawa, Wako-shi, Saitama 351-0198, Japan. [4]Department of Applied Physics, College of Applied Science, Kyung Hee University, 1732 Deogyeong-daero, Giheung-gu, Yongin-si, Gyeonggi-do 17104, South Korea. [5]Department of Physics, Korea University, 145 Anam-ro, Seoul 02841, South Korea. †Present address: JEIP, USR 3573 CNRS, Collège de France, PSL Research University, 11, place Marcelin Berthelot, 75231 Paris Cedex 05, France.
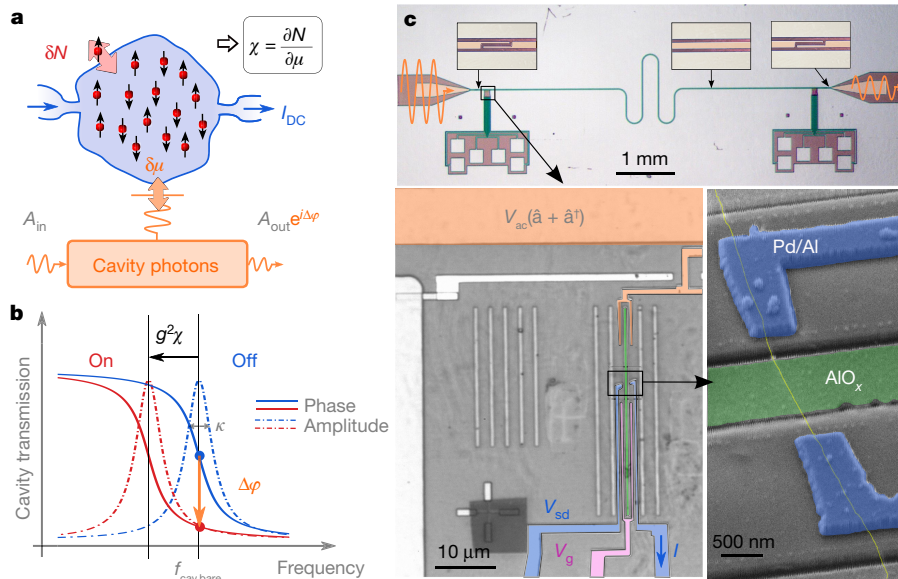
Figure 1 | Hybrid quantum dot–cavity set-up. a, The compressibility of an electron gas is associated with $\partial N/\partial \mu$, with N the mean number of electrons and μ the chemical potential. **b**, The finite compressibility χ of the electron gas shifts the resonance frequency of a microwave cavity by $g^2\chi$ (the 'on' state) from its bare resonance frequency $f_{cav,bare}$ (the 'off' state). The phase of the transmitted microwave signal at $f_{cav,bare}$ is thus shifted by $\Delta\varphi$. The constant g is the electron–photon coupling and κ is the cavity linewidth. **c**, Top, a carbon-nanotube-based quantum dot

circuit is capacitively coupled to a coplanar waveguide microwave cavity. The chemical potential of the dot is controlled by the gate voltage V_g. The source–drain bias V_{sd} is applied between the two electrodes (in blue) which delimit the quantum dot. Bottom, left, close-up view of one region corresponding to an anti-node of the electric field. Bottom, right, close-up view of a device, showing the nanotube (in yellow) above a bottom gate (in green) and connected to the contacts shown blue.

The compressibility can therefore be read out through a shift of the resonance frequency of the cavity. This yields the corresponding phase shift $\Delta\varphi = 2g^2\hbar\chi/\kappa$ for the transmitted microwave signal, where κ and g correspond respectively to the linewidth of the cavity and the electron–photon coupling strength (see Methods). The compressibility of the quantum dot depends on the linewidth of a Coulomb peak. Using a well-established theory (see Methods), we find for all the Coulomb peaks studied that $g \approx 2\pi \times (65 \pm 15\,\mathrm{MHz})$[20]. In that case, the compressibility

$\frac{\partial N}{\partial \mu}$ can also be viewed as the zero-frequency charge susceptibility, which stems from the retarded correlator $\chi(t) = -i\theta(t)[\hat{n}(t), \hat{n}(0)]$, where $\hat{n}(t)$ is the electron number operator of the dot and $\theta(t)$ is a step function (see Methods). We conclude that in the Coulomb blockade regime, both finite conductance and compressibility only arise from the ability of the mobile charges to tunnel in or out of the dot. Importantly, our circuit quantum electrodynamics architecture resolves well a very small compressibility, of the order of $1{,}000\,(\mathrm{eV})^{-1}$, corresponding to 160 aF,
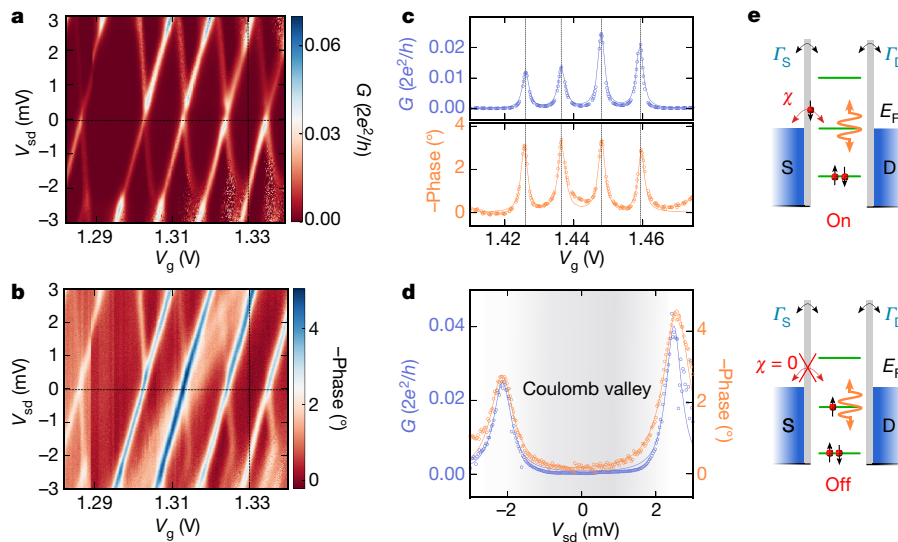

Figure 2 | Nature of the electron–photon coupling. a, b, Conductance G (**a**) and phase maps (**b**) in the V_g–V_{sd} plane for low gate voltages. The opposite phase is represented in order to map directly the microwave signal onto the compressibility. **c**, Gate sweep for $V_{sd} \approx 0$ for the conductance (top panel) and for the phase (bottom panel). The points are experimental data and the solid lines correspond to Lorentzian fits. **d**, Bias sweep at $V_g = 1.33\,\mathrm{V}$. The soft-grey-shaded area corresponds to the Coulomb valley. **e**, Coupling mechanism: the cavity photons modulate adiabatically the chemical potential of the quantum dot. The dot has

tunnelling rates Γ_S and Γ_D to the source S and the drain D, respectively. A finite dot density of states at the Fermi level E_F turns on electronic transfers between the quantum dot and the leads. This dipole induces a shift in the resonant frequency of the cavity (top panel), which leads to the phase shift seen in **b**, **c** and **d**. The electrons (red balls) carrying a spin (up or down black arrows) can hop back and forth from the green energy levels to the blue reservoirs ('on', top panel). The 'off' situation (bottom panel) corresponds to the case where a green level is not aligned with the Fermi energy of the blue reservoir.
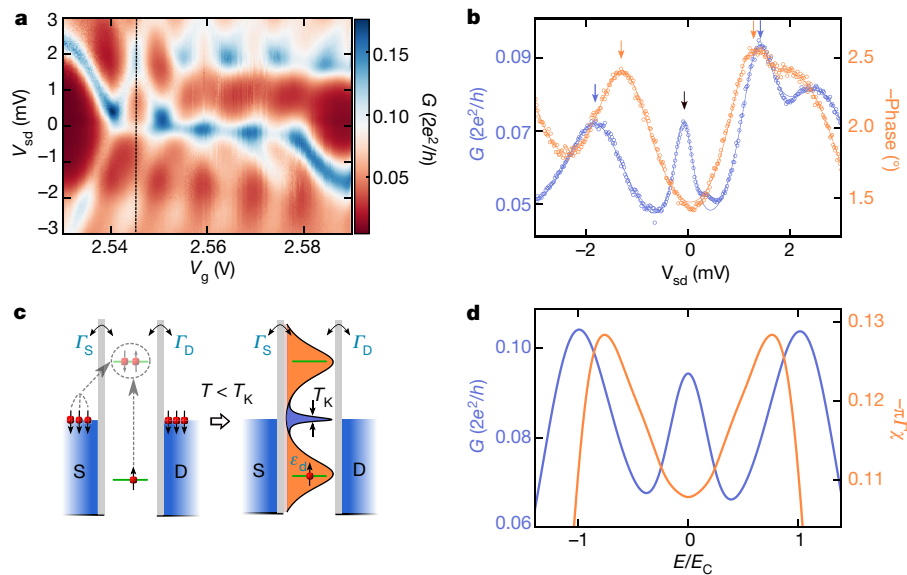
Figure 3 | Transparent Kondo resonance. a, Conductance map in the Kondo regime. See main text. **b**, Simultaneous bias dependence of the conductance and the phase in the middle of a Kondo ridge along the black dashed line in **a**. The blue (orange) arrows mark the charge peaks in the conductance (compressibility). The black arrow marks the Kondo resonance. **c**, A quantum dot level away from the Fermi energy leads to a Kondo resonance through a sum of virtual processes (dashed lines). **d**, Numerical renormalization group (NRG) data corresponding to the situation in **b**. The excitation energy E is scaled by the charging energy and the compressibility by $\pi\Gamma$. Both the absence of a Kondo peak in the compressibility as well as the shift of the high-energy charge peaks between compressibility and conductance are reproduced. The corresponding parameters are $\Gamma = 0.4E_C$ (as extracted from the data) and $T = 10T_K$.

with about 1 aF resolution. This is about seven orders of magnitude smaller than the compressibility of a piece of metal of volume $1\,\mu m^3$. Remarkably, our sensitivity corresponds to a charge of about $2.5 \times 10^{-4}e$, which is about an order of magnitude lower than the charge sensitivity of an RF-SET (radio frequency single-electron transistor) set-up[21] and three orders of magnitude lower than for low-frequency techniques[10,11].

The physics becomes notably different in the Kondo regime. For that purpose, we tune the gate of the device to gate voltage $V_g \approx 2.5\,V$, where the line width of the Coulomb peak $\Gamma \approx 1\,meV$ and the charging energy $E_C \approx 2.25\,meV$. As shown in Fig. 3a, the conductance colour-scale plot displays softer Coulomb diamonds with horizontal Kondo ridges close to zero bias. The observation of several adjacent Kondo ridges is consistent with previous observations in carbon nanotubes[16]. It arises from the existence of additional degeneracies besides the spin in the spectrum of the nanotube. From the width of the zero-bias peaks, we can estimate a Kondo temperature of about 5 K. The main result of this Letter is presented in Fig. 3b. Whereas there is a finite zero-bias peak in the conductance (and therefore in the density of states of the dot), the simultaneously measured phase contrast shows that this density of states does not contribute to the compressibility (see Methods, and see Extended Data Fig. 3 for the complete compressibility map). Importantly, the high-energy charge peaks at about $\pm 2\,mV$ remain both in the phase and in the conductance, although they do not fully coincide. These experimental results are robust, because we observe them for all the Kondo ridges studied (we present 15 examples in Methods).

Our experimental findings are well reproduced by numerical renormalization group (NRG) calculations of the χ and the dot density of states $\nu(E)$, where E is the energy. The latter can be directly mapped onto the conductance $G(eV_{sd})$, plotted in Fig. 3d, by making the identification $E = eV_{sd}$, thanks to the small height of the Kondo peak (about $0.12 \times 2e^2/h$), which ensures that the dot is much more tunnel coupled to one of the two reservoirs. The low-bias data directly show that a finite (DC) current flows through the device, although the charge in the QD is frozen[4–6].

We can explain this feature within the Kondo model, as illustrated in Fig. 3c. When a QD degenerate level is singly occupied by a frozen charge, an antiferromagnetic coupling appears between the single electron and the conduction electrons at the Fermi energy. The emergent many-body state does not contribute to the compressibility, because it arises from virtual tunnelling processes. Therefore, our measurements strongly suggest that the Kondo resonance in the conductance, also called Abrikosov–Suhl–Nagaoka resonance, is associated with the fluctuations of the spin degree of freedom, whereas the charge fluctuations in the dot are frozen. Interestingly, the NRG
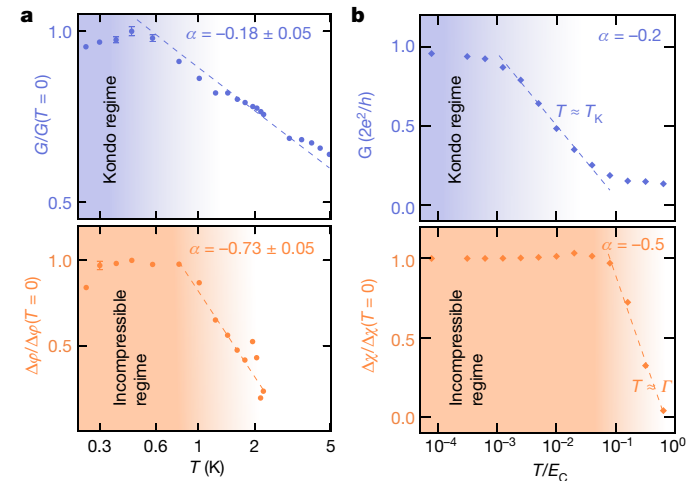

Figure 4 | Temperature dependence of conductance and compressibility. a, Temperature dependence of the conductance (top panel) and the phase (bottom panel) on the Kondo ridge at ($V_g \approx 2.567\,V$, $V_{sd} \approx -0.15\,mV$) (see Methods and Extended Data Fig. 6). In order to compensate thermal drifts, the phase shift signal $\Delta\varphi$ on the Kondo ridge is measured with respect to the right adjacent Coulomb peak at a given temperature. The error bars, corresponding to the systematic errors in our measurements, are about the size of these experimental points. The dashed lines show a linear fit on a logarithmic scale that corresponds to a logarithmic law $\alpha\log(T)$; the value of α is shown. **b**, NRG data as a function of temperature, for $\Gamma = 0.4E_C$ (as extracted from the data). The dashed lines show a linear fit on a logarithmic scale that corresponds to a logarithmic law $\alpha\log(T)$; the value of α is shown. The conductance displays a 'down turn' at $T \approx T_K$, whereas $\Delta\varphi$ displays a down turn at $T \approx \Gamma$.

data are also able to reproduce the shift between the conductance and compressibility charge peaks around $\pm 2\,\mathrm{mV}$. We speculate that this might be a correlation effect related to an interaction-driven renormalization of the system parameters.

The temperature dependence of the cavity and transport signals further confirms that the conductance and the compressibility obey different physical principles governed by different energy scales. When the temperature increases, the many-body Kondo resonance decreases logarithmically on a temperature scale set by T_K, as shown in Fig. 4a. The residual compressibility χ_V in the valley evolves on a temperature scale that is different from that of the many-body Kondo resonance, as it is simply due to single-electron tunnelling and set by Γ (explicitly, $\chi_V \approx -0.13/(\pi\Gamma)$ at $T = 0$ from the NRG data). A linear fit to the data plotted on a logarithmic–linear scale in the high-temperature range gives a logarithmic law of about $-0.18\log(T/T_K)$ for the conductance and of about $-0.73\log(T/\Gamma)$ for the compressibility. In Fig. 4b, we show the corresponding plots obtained by NRG. We find that they are in good agreement with the experimental data. In particular, the NRG data in Fig. 4b indicate that the temperature dependence for the conductance is governed by T_K whereas for the compressibility it is governed by Γ. It is important to note however that extracting the value of Γ from our experimental data accurately is not straightforward here because the apparent spectral ($\mathrm{d}I/\mathrm{d}V$, where I is current and V is voltage) width of the charge resonance has been observed to depend on interaction (see Methods). This is also seen in the NRG data in Fig. 3d. This can explain why the temperature scale for the down-turns for the conductance and the compressibility are less separated in our experimental data than in the NRG data. Nevertheless, both the distinct slopes and the separate down-turns show that the conductance and the compressibility are affected by temperature with different mechanisms. This stems directly from the decoupling of the charge and spin degrees of freedom in a Kondo cloud.

We have directly observed the freezing of charge dynamics which is a crucial feature of a Kondo resonance. Our dual conductance/compressibility measurements illustrate the fundamental difference between a Kondo resonance and a simple resonant level where many body effects are absent.

Our set-up could be generalized to many types of mesoscopic circuits[22–24] and could be transposed to the optical domain to probe the compressibility of other types of conductors. It could be used to study some important fermion–boson problems in a controlled manner. Electron–phonon interactions in solids could be simulated by using the analogy between phonons and the photons in our cavity. Furthermore, the cavity photons are slow here with respect to the electrons of the dot ($hf_{\mathrm{cav}} \ll E_C, \Gamma, k_B T_K$): this situation has allowed us to probe non-invasively the low-frequency charge dynamics of the QD, which are relevant to understanding the DC properties of our system. We expect to access dynamical aspects of tunnelling[14,25] and Kondo physics if one of the above-mentioned inequalities is not fulfilled. Finally, the sudden injection of a coherent field into the cavity could perform a quantum quench of the system, which could give interesting insights into the dynamics of the Kondo cloud.

Online Content Methods, along with any additional Extended Data display items and Source Data, are available in the online version of the paper; references unique to these sections appear only in the online paper.

1. Goldhaber-Gordon, D. *et al.* Kondo effect in a single-electron transistor. *Nature* **391,** 156–159 (1998).
2. Nygard, J., Cobden, D. H. & Lindelof, P. E. Kondo physics in carbon nanotubes. *Nature* **408,** 342 (2000).
3. Roch, N. *et al.* Quantum phase transition in a single-molecule quantum dot. *Nature* **453,** 633 (2008).
4. Hewson, A. C. *The Kondo Problem to Heavy Fermions* (Cambridge Univ. Press, 1993).
5. Lee, M., Lopez, R. Choi, M.-S., Jonckheere, T. & Martin, T. Many-body correlation effect on mesoscopic charge relaxation. *Phys. Rev. B* **83,** 201304(R) (2011).
6. Filippone, M., Le Hur, K. & Mora, C. Giant charge relaxation resistance in the Anderson model. *Phys. Rev. Lett.* **107,** 176601 (2011).
7. Iftikhar, Z. *et al.* Two-channel Kondo effect and renormalization flow with macroscopic quantum charge states. *Nature* **526,** 233 (2015).
8. Keller, A. J. *et al.* Universal Fermi liquid crossover and quantum criticality in a mesoscopic device. *Nature* **526,** 237 (2015).
9. Georges, A., Kotliar, G., Krauth, W. & Rozenberg, M. J. Dynamical mean-field theory of strongly correlated fermion systems and the limit of infinite dimensions. *Rev. Mod. Phys.* **68,** 13 (1996).
10. Ashoori, R. C. *et al.* Single-electron capacitance spectroscopy of discrete quantum levels. *Phys. Rev. Lett.* **68,** 3088 (1992).
11. Ilani, S., Donev, L. A. K., Kindermann, M. & McEuen, P. L. Measurement of the quantum capacitance of interacting electrons in carbon nanotubes. *Nat. Phys.* **2,** 687 (2006).
12. Deblock, R., Noat, Y., Bouchiat, H., Reulet, B. & Mailly, D. Measurements of flux dependent screening in Aharonov-Bohm rings. *Phys. Rev. Lett.* **84,** 5379 (2000).
13. Gabelli, J. *et al.* Violation of Kirchhoff's laws for a coherent RC circuit. *Science* **313,** 499 (2006).
14. Bruhat, L. E. *et al.* Cavity photons as a probe for charge relaxation resistance and photon emission in a quantum dot coupled to normal and superconducting continua. *Phys. Rev. X* **6,** 021014 (2016).
15. Viennot, J. J., Palomo, J. & Kontos, T. Stamping single wall nanotubes for circuit quantum electrodynamics. *Appl. Phys. Lett.* **104,** 113108 (2014).
16. Laird, E. *et al.* Quantum transport in carbon nanotubes. *Rev. Mod. Phys.* **87,** 703 (2015).
17. Büttiker, M., Prêtre, A. & Thomas, H. Mesoscopic capacitors. *Phys. Lett. A* **180,** 364 (1993).
18. Prêtre, A., Thomas, H. & Büttiker, M. Dynamic admittance of mesoscopic conductors: discrete-potential model. *Phys. Rev. B* **54,** 8130 (1996).
19. Cottet, A., Kontos, T. & Douçot, B. Electron-photon coupling in mesoscopic quantum electrodynamics. *Phys. Rev. B* **91,** 205417 (2015).
20. Delbecq, M. R. *et al.* Coupling a quantum dot, fermionic leads and a microwave cavity on a chip. *Phys. Rev. Lett.* **107,** 256804 (2011).
21. Lehnert, K. W. *et al.* Quantum charge fluctuations and the polarizability of the single-electron box. *Phys. Rev. Lett.* **91,** 106801 (2003).
22. Frey, T. *et al.* Dipole coupling of a double quantum dot to a microwave resonator. *Phys. Rev. Lett.* **108,** 046807 (2012).
23. Petersson, K. D. *et al.* Circuit quantum electrodynamics with a spin qubit. *Nature* **490,** 380 (2012).
24. Viennot, J. J., Dartiailh, M. C., Cottet, A. & Kontos, T. Coherent coupling of a single spin to microwave cavity photons. *Science* **349,** 408 (2015).
25. Frey, T. *et al.* Quantum dot admittance probed at microwave frequencies with an on-chip resonator. *Phys. Rev. B* **86,** 115303 (2012).

Author Contributions M.M.D. set up the experiment, made the devices and carried out the measurements with the help of T.K. M.M.D. performed the analysis of the data with input from T.K. J.J.V., M.C.D., L.E.B. and M.R.D. contributed through early experiments and development of the nanofabrication process. M.C.D. developed the data acquisition software. M.L. and M.S.C. carried out the NRG calculations. M.M.D., T.K. and A.C. carried out the semi-classical theory of dot–cavity coupling. T.K., A.C. and M.M.D. co-wrote the manuscript with input from all authors.

METHODS

Fabrication of devices and measurement techniques. A 150-nm-thick Nb film is first evaporated on an Si substrate that is suitable for RF measurements at a rate of 1 nm s^{-1} and at a pressure of 10^{-9} mbar. The cavity is made subsequently using photolithography combined with reactive ion etching (SF$_6$ process). An array of bottom gates is then made with two e-beam lithography steps in a 100 μm square opening of cavity ground plane near the central conductor. First, we etch 750 nm × 25 μm trenches of 130 nm depth with reactive ion etching (CHF$_3$ process). Second, we deposit inside the trenches 150 nm narrower layers of Ni(100 nm)/AlOx(6 nm). The Al oxide is obtained by 3 steps of static oxidation of 2-nm-thick Al layers using an O$_2$ pressure of 1 mbar for 10 min. Carbon nanotubes are grown with chemical vapour deposition technique (CVD) at about 900 °C using a methane process on a separate quartz substrate and stamped above the bottom gates[15]. The nanotubes are then localized and those which correctly lie on a bottom gate are contacted with Pd(4 nm)/Al(80 nm). During this last e-beam lithography and evaporation step, gate electrodes are also patterned in order to couple capacitively the bottom gate to a DC gate voltage V_g and to the AC potential of the central conductor of the cavity.

The DC measurements are carried out using standard lock-in detection techniques with a modulation frequency of 77 Hz and an amplitude of 30 μV. The base temperature of the experiment is 255 mK. The microwave measurements are carried out using room temperature microwave amplifiers with a total gain of 60 dB. We measure both quadratures of the transmitted microwave signal using an I–Q mixer and low frequency modulation at 2.7 kHz. The cavity resonance frequency is 6.67129 GHz and its quality factor is between 10,000 and 20,000 depending on the run of our single shot ^{3}He cryostat (see Extended Data Fig. 1). The input power for the cavity is -89 ± 2 dBm resulting in an average photon number of about 30,000. This power yields a microwave modulation of about 40 μV which ensures that we are in the linear regime (consistent with the power dependence of the DC conductance; see below).

Link between the phase shift of the microwave signal and the compressibility. The transmission of the cavity in the frequency domain is shifted by $\hbar g^2 \chi / 2\pi$, where χ is the compressibility and g the electron–photon coupling constant (see below):

$$T(f) = \frac{-i\kappa/2}{2\pi(f - f_{\mathrm{cav}}) + \frac{i\kappa}{2} - \hbar g^2 \chi}$$

where f is the frequency, f_{cav} the resonance frequency of the cavity and κ is the linewidth of the cavity.

We measure the transmission at resonance $f = f_{\mathrm{cav}}$. This yields:

$$T(f) = \frac{A_{\mathrm{out}} \mathrm{e}^{i\Delta\varphi}}{A_{\mathrm{in}}} = \frac{-i\kappa/2}{\frac{i\kappa}{2} - \hbar g^2 \chi}$$

where A_{out}, A_{in} and $\Delta\varphi$ are respectively the input amplitude, the output amplitude and the phase between the output and the input of the microwave field transmitted through the cavity. Hence, for small phase shifts, and making the substitution i to $-i$ for the engineering convention,

$$\Delta\varphi \approx 2g^2 \hbar \chi / \kappa$$

This expression holds for any electronic system as long as the linear and adiabatic regime are reached. The parameter $\kappa \approx 2\pi \times 0.3$ MHz, yielding a quality factor $Q = 2\pi f_{\mathrm{cav}}/\kappa = 18,000$, can be measured directly from the transmission spectrum of the cavity (Fig. 1b). At low temperatures, in the simplest case, the compressibility reads: $\chi = \frac{\partial N}{\partial \varepsilon_d} = -\frac{2}{\pi} \frac{\Gamma}{\Gamma^2 + 4\varepsilon_d^2}$, where Γ and ε_d are respectively the line width of the Coulomb peak and the position of the dot energy level. The dot's parameter $\Gamma = \Gamma_{\mathrm{S}} + \Gamma_{\mathrm{D}}$, with $\Gamma_{\mathrm{S}} = 0.7$ meV and $\Gamma_{\mathrm{D}} = 4$ μeV can be determined from the conductance measurements (see Fig. 2) which also allow us to extract the charging energy $E_{\mathrm{C}} = 3.5$ meV. As a consequence, the joint conductance/phase measurements presented in Fig. 2c allow us to directly determine the electron–photon coupling constant g on each Coulomb peak, $g \approx 2\pi \times (65 \text{ MHz} \pm 15 \text{ MHz})$. The negative sign observed for the phase contrast shows directly that the dot reduces the frequency of the resonator. Therefore, the effective admittance of the QD circuit is that of an effective capacitance in parallel with the capacitance of resonator. This stems from the fact that cavity photons are coupled to the gate (and therefore ε_d), but not to the source–drain contacts. This feature of our set-up is crucial to ensure that we measure only the compressibility of the electron system in the quantum dot, which was not the case in a previous experiment in the Kondo regime[17] (see below for a discussion).

The large coupling strength found is consistent with our circuit design, shown in Fig. 1c, where a bottom gate (in green) very close to the single wall carbon nanotube combines the AC voltage of the central conductor of the cavity and the DC gate voltage (see below). The electron–photon coupling constant simply reads:

$\hbar g = e\alpha V_{\mathrm{rms}}$ ($e > 0$), where V_{rms} is the root mean square voltage associated with a single photon and α the ratio of the induced RF oscillations of the dot's chemical potential to the potential of the central conductor. From the conductance map, we can infer the DC lever arm to be about 0.3. From our gate layout (Fig. 1c), we can estimate that the AC capacitance is about 3 times smaller than the DC capacitance. This leads to $\alpha \approx 0.1$, so that $g \approx 2\pi \times 50$ MHz, using $V_{\mathrm{rms}} \approx 2$ μV. This order of magnitude is in good agreement with our experimentally determined coupling strength of about $2\pi \times (50$–100 MHz$)$.

Conductance and microwave phase in the Coulomb blockade regime over a wide gate voltage range. The cavity resonance which is used to perform our compressibility measurements is presented in Extended Data Fig. 1 left panel. We show in Extended Data Fig. 2 the phase contrast and the conductance as a function of the gate voltage at zero bias in the Coulomb blockade regime on a wide gate voltage range. The conductance (in blue lines) displays regularly spaced Coulomb peaks with the expected fourfold periodic shell filling of low-disordered single wall carbon nanotubes. The corresponding phase of the transmitted microwave signal exhibits a pattern which is very well correlated with the conductance. The phase contrast ranges from 1° to 5° probably owing to modifications of the dot electronic wavefunctions due to weak disorder. Nevertheless, the extracted value for the coupling strength remains about $2\pi \times (50$–100 MHz$)$.

Phase colour-scale plot in the Kondo regime. We show in Extended Data Fig. 3 the phase colour-scale plot measured simultaneously with the conductance colour-scale plot shown in Fig. 3a. Similarly to the Coulomb blockade regime (Fig. 2b), the phase contrast is bigger for the left tilted edges of the Coulomb diamonds (the tilted black lines are guides to the eye). The latter are blurred as expected because the Kondo regime corresponds to a gate region with larger values of Γ. There are some phase resonances which are not correlated with the Coulomb diamond edges, as in the area around ($V_{\mathrm{sd}} = -2$ mV, $V_g = 2.54$ V). We attribute this effect to spurious impurity levels that are coupled to the cavity. Importantly, the Kondo ridges that are clearly visible in the colour map of the conductance are completely absent from the phase map.

Phase and conductance for additional Kondo ridges. We show in this section the robustness of our findings. We present the dual conductance and compressibility cuts as a function of V_{sd} for 15 Kondo ridges in Extended Data Fig. 4. These cuts correspond to the dashed lines represented on the colour-scale plots of Extended Data Fig. 5 (for 13 out of the 15 cuts). The cuts for the second and the fourth ridge, shown in Extended Data Fig. 3 which corresponds to the phase contrast for Fig. 3a, are also presented in this panel of 15 cuts. Essentially all that is described for the Kondo ridge treated in the main text is observed in Extended Data Fig 4. The Kondo peak is present in the conductance (in blue) but not in the compressibility (in orange). This further confirms the robustness of our findings.

We also present in Extended Data Fig. 6 the temperature dependence of the joint conductance and compressibility for the second and fourth ridge in Fig. 3a. The slope of the fourth conductance ridge is found to be around -0.15 (Extended Data Fig. 6b, top), close to the value for the third ridge presented in the main text in Fig. 4a. The slope of the second conductance ridge (Extended Data Fig. 6a, top) is more difficult to estimate, as can be seen from the spread of the data points probably arising from small gate drifts as we increase the temperature. It is even more difficult for the data of the first ridge (corresponding to the cut presented in the main text in Fig. 3a) and this is why we do not present it. The compressibility in both Extended Data Fig. 6a and Extended Data Fig. 6b is shown to start to decrease after the down-turn in the conductance, as highlighted by the blue and orange regions. This is clearer in Extended Data Fig. 6b than in Extended Data Fig. 6a, probably because of the larger spread in the compressibility measurements in the latter. Note that both slopes for compressibility are different from what is presented in the main text in Fig. 4a. This is expected because the slope for the compressibility is not universal and depends on Γ.

Phase and conductance for the Kondo ridge used in Fig. 4. We show in Extended Data Fig. 7 the dual conductance/compressibility measurements for the gate voltage at the centre of the third Kondo ridge in Fig. 3a. The same features as in Fig. 3 are observed. Although a peak is visible in the conductance, signalling the Kondo resonance, it is absent from the compressibility. The charge peaks are still visible in both measurements, around ± 2 mV. As for the example in the main text in Fig. 3b, the finite bias charge peaks are not fully correlated.

In order to obtain the temperature dependence of $\Delta\varphi$ in Fig. 4a, we use gate scans for $V_{\mathrm{sd}} = 0$ mV at different temperatures as shown in Extended Data Fig. 7 right panel. As described in the main text, the right adjacent Coulomb peak is used as a reference for the phase. In addition, in order to get a meaningful temperature dependence of the phase, we rescale the data by the relative variations of the quality factor of the cavity measured at each temperature (see Extended Data Fig. 1 right panel for the temperature dependence of the linewidth of the cavity).

Theory of cavity–quantum dot coupling in the adiabatic regime. We present in this section the general theory describing the cavity response in the presence

of a quantum dot with various light–matter coupling schemes. The most general Hamiltonian describing the hybrid quantum dot cavity system is[19]:

$$\hat{H} = \hbar\omega_{\text{cav}}\, \hat{a}^{\dagger}\hat{a} + (\hbar g\hat{n} + \hbar g_{\text{S}}\,\hat{n}_{\text{S}} + \hbar g_{\text{D}}\hat{n}_{\text{D}})(\hat{a} + \hat{a}^{\dagger}) + \hat{H}_{\text{dot}} + \hat{H}_{\text{tunnel dot/lead}}$$
$$+ \hat{H}_{\text{Baths}}$$

where ω_{cav} is the pulsation of the cavity and $\hat{a}^{\dagger}$ ($\hat{a}$) the creation (annihilation) operators for the cavity photons and $\hat{n}$ the number of electrons in the dot. The coupling term includes the charge on the dot characterized by the operator $\hat{n}$ as well as the number of electrons in the source (S) and drain (D) reservoirs characterized by operators $\hat{n}_{\text{S(D)}}$. As we will see below, the existence of these different couplings have specific consequences for the cavity signals. It is therefore possible to infer which term dominates in order to demonstrate that the compressibility of the dot is directly measured.

It is now useful to define $\hat{n}_{+/-} = \hat{n}_{\text{S}} \pm \hat{n}_{\text{D}}$. Charge conservation imposes the conservation of $\hat{n}_{+} + \hat{n}$. We consider an excitation of the cavity with the form: $\langle \hat{b}_{\text{in}}\rangle = b_{\text{in}}^{0}(t)e^{-i2\pi ft}$, with $f \approx f_{\text{cav}}$. There are a few thousand photons in the cavity so we can use the semi-classical approximation for the photonic field. The equation of motion of the amplitude $\langle \hat{a}\rangle = \bar{a}(t)e^{-i2\pi ft}$ of the field in the semiclassical limit reads:

$$\dot{\bar{a}} = [i2\pi(f - f_{\text{cav}}) - \kappa/2]\bar{a} - ig_{+}N - ig_{-}N_{-} - \sqrt{\kappa_{\text{in}}}b_{\text{in}} \tag{1}$$

with $N = \langle \hat{n}\rangle$, and $N_{-} = \langle \hat{n}_{-}\rangle, g_{+} = g - \frac{g_{\text{S}} + g_{\text{D}}}{2}$ and $g_{-} = g - \frac{g_{\text{S}} - g_{\text{D}}}{2}$ In the stationary regime, the cavity field reads[2]:

$$\bar{a} = \frac{-i\sqrt{\kappa_{\text{in}}}b_{\text{in}}}{2\pi(f - f_{\text{cav}}) + i\frac{\kappa}{2} - \hbar\sum_{ij\in\{+,-\}}g_{i}g_{j}\chi_{ij}(f)} \tag{2}$$

The susceptibilities $\chi_{ij}(f)$ are the Fourier transforms of: $\chi_{ij}(t) = -i\theta(t)[\hat{n}_{i}(t), \hat{n}_{j}(0)]$:

$$\chi_{ij}(f) = \int_{-\infty}^{+\infty}dt\chi_{ij}(t)e^{i2\pi ft} \tag{3}$$

In general, all these susceptibilities depend on the frequency. However, when the frequency of the cavity is much smaller than all the characteristic frequencies involved in the dynamics of the dot (essentially $\Gamma_{\text{S(D)}}$ in the single dot case), one may use the adiabatic limit of $\chi_{ij}(f)$, that is, $\chi_{ij}(f \to 0)$. Since $\hat{n}$ couples to the energy level ε_{d} and $\hat{n}_{-}$ couples to the source-drain bias and is $\frac{2I}{-i2\pi fe}$, where I is the average current, one may write:

$$\sum_{ij\in\{+,-\}}g_{i}g_{j}\chi_{ij}(f) = g_{+}^{2}\frac{\partial N}{\partial \epsilon_{\text{d}}} + g_{-}^{2}\frac{4}{e^{2}}\frac{1}{i2\pi f}\frac{\partial I}{\partial V_{\text{ac}}} - 2g_{-}g_{+}\frac{\partial N}{\partial eV_{\text{ac}}}$$
$$+ 2g_{+}g_{-}\frac{1}{e}\frac{1}{i2\pi f}\frac{\partial I}{\partial \epsilon_{\text{d}}} \tag{4}$$

with $N = \langle \hat{n}\rangle$ For $V_{\text{sd}} = 0$, the current I is zero independently of ϵ_{d}, which implies that the last term in the above equation is zero. The quantities $\frac{\partial I}{\partial V_{\text{ac}}}$ and $\frac{\partial N}{\partial V_{\text{ac}}}$ are the derivatives of the current and the charge of the dot when the bias is applied symmetrically since the perturbation is proportional to $\hat{n}_{-}$. The second term is purely imaginary since $\frac{\partial I}{\partial V_{\text{ac}}}$ is real. However, one can see that $\frac{\partial N}{\partial V_{\text{ac}}}$ can also contribute to the real part of the response and therefore to the phase shift with prefactor $g_{-}g_{+}$. It is therefore important to assess that the dominant response comes from the $g_{+}^{2}\frac{\partial N}{\partial \epsilon_{\text{d}}}$ term which corresponds to $g_{+}^{2}\chi$, where χ is the compressibility defined in the main text (note that here we have replaced μ of the main text by ε_{d} to make connection with the common notation of the quantum dot Hamiltonian where ε_{d} is the position of the electron level). For that purpose, we use the second (dissipative) term and the fact that its derivation is valid for any circuit in the adiabatic regime. The Kondo peak is absent from the amplitude data (not shown) to the experimental uncertainty of 0.001: this implies that $g_{-} < 2\pi \times 2.0$ MHz for example for the peak shown in Extended Data Fig. 7. This is more than an order of magnitude smaller than g_{+}.

It is instructive to evaluate the general form of the dot response in the adiabatic and non-interacting regime. We may define:

$$\chi_{0}(\varepsilon_{\text{d}}) = -\int \frac{d\varepsilon}{2\pi}\mathcal{A}(\varepsilon - \varepsilon_{\text{d}})\frac{1}{4k_{\text{B}}T\cosh^{2}\left(\frac{\varepsilon}{2k_{\text{B}}T}\right)} \tag{5}$$

where $\mathcal{A}(\varepsilon - \varepsilon_{\text{d}})$ is the density of states of the dot. Using for example the Keldsyh formalism, we get:

$$\frac{\partial N}{\partial \varepsilon_{\text{d}}} = \Gamma_{\text{S}}\chi_{0}(\varepsilon_{\text{d}} - eV_{\text{S}}) + \Gamma_{\text{D}}\chi_{0}(\varepsilon_{\text{d}} - eV_{\text{D}}) \tag{6}$$

$$\frac{\partial N}{\partial \varepsilon_{\text{a}}} = -\Gamma_{\text{S}}\chi_{0}(\varepsilon_{\text{d}} - eV_{\text{S}}) + \Gamma_{\text{D}}\chi_{0}(\varepsilon_{\text{d}} - eV_{\text{D}}) \tag{7}$$

$$\frac{\partial I}{\partial \varepsilon_{\text{d}}} = \Gamma_{\text{S}}\Gamma_{\text{D}}[\chi_{0}(\varepsilon_{\text{d}} - eV_{\text{S}}) - \chi_{0}(\varepsilon_{\text{d}} - eV_{\text{D}})] \tag{8}$$

$$\frac{\partial I}{\partial \varepsilon_{\text{a}}} = \Gamma_{\text{S}}\Gamma_{\text{D}}[-\chi_{0}(\varepsilon_{\text{d}} - eV_{\text{S}}) - \chi_{0}(\varepsilon_{\text{d}} - eV_{\text{D}})] \tag{9}$$

Where ϵ_{a} correspond to the antisymmetric modulation $V_{\text{S}} = -V_{\text{D}} = \frac{\varepsilon_{\text{a}}}{-e} = \frac{V_{\text{ac}}}{2}$

The above expressions show the equivalence between a compressibility measurement and a conductance measurement in the non-interacting regime.

Alternative scenario for the 'transparent' Kondo resonance. In the Kondo regime, we have seen that the conductance peak at zero bias is absent from the cavity signal. Could this conductance peak be attributed to another level, pinned at zero bias, with a chemical potential ε'_{d} which is not coupled to the cavity?

From the bias dependence, this level has a width $\Gamma' = k_{\text{B}}T_{K}$. Its conductance appears and disappears at some gate voltage V_{g}. The conductance depends only on the chemical potential and Γ' of the level. As the chemical potential is not coupled to the cavity, the gate has also no influence on it, so $\frac{\partial \varepsilon'_{\text{d}}}{\partial V_{\text{g}}} \approx 0$. Therefore, the level should have at least one of its Γ', for example Γ'_{D}, that depends on the gate: $\frac{\partial \Gamma'_{\text{D}}}{\partial V_{\text{g}}} \neq 0$.

The conductance appears as a Lorentzian with respect to the bias voltage V_{SD}, so the charge number N' is:

$$N' = \frac{1}{2} - \frac{1}{\pi}\arctan\frac{2eV_{\text{SD}}}{\Gamma'_{\text{S}} + \Gamma'_{\text{D}}} \tag{10}$$

Its derivative with respect to the gate is then:

$$\frac{\partial N'}{\partial V_{\text{g}}} = \frac{1}{\pi}\frac{\Gamma'_{\text{S}} + \Gamma'_{\text{D}}}{4(eV_{\text{SD}})^{2} + (\Gamma'_{\text{S}} + \Gamma'_{\text{D}})^{2}}\frac{2eV_{\text{SD}}}{\Gamma'_{\text{S}} + \Gamma'_{\text{D}}}\frac{\partial \Gamma'_{\text{D}}}{\partial V_{\text{g}}} \tag{11}$$

For a coupling to the dot chemical potential, we have $\frac{\partial N}{\partial V_{\text{g}}} = \frac{\partial \varepsilon_{\text{d}}}{\partial V_{\text{g}}}\frac{\partial N}{\partial \epsilon_{\text{d}}} = \alpha\chi$, where χ is the compressibility and α the lever arm. By analogy, $\frac{\partial \Gamma'_{\text{D}}}{\partial V_{\text{g}}}$ is the lever arm α' that enters in the coupling parameter g' describing the response of the level to a modulation of Γ'_{D}. From the conductance data, one can estimate that this lever arm is 0.75 smaller than the lever arm α of the level that gives the Coulomb peaks. Therefore the phase should be shifted at the end of each Kondo ridge by the same amount as for the Coulomb peaks. Our set-up can therefore exclude such a situation without the need for extra knowledge of the system.

Figure of merit of our compressibility measurements. Here we describe in greater detail than in the main text the figure of merit of our compressibility measurement set-up. Two main features are important for defining the figure of merit: first, the effective capacitance resolution δC which can be achieved, and second, the maximum excitation voltage which is used for that measurement δV. The latter is crucial for keeping the linearity of our detection scheme. These two parameters enter into the charge resolution of the set-up: $\mathcal{N} = \delta C \times \delta V/e$. In our case, since we estimate $\delta C \approx 1$ aF from our phase noise of about 0.01 degree and we estimate $\delta V \approx 40\,\mu$V from the average number of photons in our cavity, this leads to $\mathcal{N} \approx 2.5 \times 10^{-4}e$. As a comparison, the minimum δC in ref. 8 is 1 aF but with a δV of about 20 mV.

Photon number dependence of the differential conductance in the Coulomb blockade regime. In this section, we show that one can estimate the electron–photon coupling strength with a method complementary to that used in the main text, from the microwave power dependence of the conductance. For a coupling to the gate, and in the adiabatic case $f_{\text{cav}} \ll \Gamma$, the conductance is modulated by the cavity photons as:

$$G(t) = G(\varepsilon_{d} + 2\hbar g\sqrt{\bar{n}}\,\cos(2\pi f_{\text{cav}}t)) \tag{12}$$

where $\bar{n}$ is the average photon number. The conductance is a Lorentzian with a width Γ, hence, at $\varepsilon_{\text{d}} = 0$, a DC measurement gives:

$$G = \int_{0}^{2\pi}\frac{d\theta}{2\pi}G(2\hbar g\sqrt{\bar{n}}\,\cos(\theta)) = \frac{1}{\sqrt{1 + 16\bar{n}(\hbar g/\Gamma)^{2}}} \tag{13}$$

The mean number of photon depends on the cavity input power and its transmission:

$$\bar{n} = \frac{10^{\frac{P_{IF}+S_{att}}{10}+\frac{S_{cav}}{20}-3}}{\pi \kappa h f_{cav}}$$ (14)

P_{IF} is the power in dBm corresponding to the root mean square amplitude V_{IF} of the low-frequency microwave modulation. S_{att} is the attenuation of RF lines to the cavity, calibrated to -82 ± 2 dB and S_{cav} the transmission of the cavity, -16 dB. This allows us to calibrate the coupling constant $g \approx 2\pi \times 60$ MHz, which is in good agreement with the one deduced from the height of the Coulomb peaks: $g^2 \approx \frac{\pi}{4} \times \Delta\varphi\Gamma\kappa/\hbar$, as shown in the right panels of Extended Data Fig. 8.

Numerical renormalization group (NRG) calculations. We calculate the compressibility using the numerical renormalization group (NRG) method[26–28]. We have adopted the Anderson impurity model:

$$H = \sum_{k\sigma} \varepsilon_k c_{k\sigma}^\dagger c_{k\sigma} + \sum_\sigma \varepsilon_d d_\sigma^\dagger d_\sigma + U n_\downarrow n_\uparrow + \sum_{k\sigma} t_k c_{k\sigma}^\dagger d_\sigma + \text{h.c.}$$

where $c_{k\sigma}^\dagger$ and $c_{k\sigma}$ are the annihilation and creation operators, respectively, of the conduction electrons with momentum k and spin σ, whose energy is ε_k, and $d_\sigma^\dagger$ and d_σ are the same operators for the electrons on the quantum dot, whose energy is ϵ_d. U describes the Coulomb interaction on the dot and $n_\sigma = d_\sigma^\dagger d_\sigma$. Note that in the orthodox charging model, $U \approx 2E_C$ ($E_C = e^2/2C$ with C being the capacitance of the dot). In experiments, the tunnelling amplitude t_k is assessed through the level hybridization (or tunnelling-rate) parameter: $\Gamma(E) = \pi \sum_k |t_k|^2 \delta(E - \epsilon_k)$. Assuming sufficiently wide conduction band, the energy-dependence in $\Gamma(E)$ is ignored.

As the NRG method works only at equilibrium, we adopt the approximation $\chi(f \approx 0, V = V_{sd}) \approx \chi_{NRG}\left(E = \frac{eV_{sd}}{\hbar}, V = 0\right)$ which is reasonably good in the linear-response regime and static limit $f_{cav} \ll T_K$. Direct application of the dynamical NRG method[26,27] gives the imaginary part, $\text{Im}(\chi)$ of the zero-bias compressibility $\chi(E) \equiv \chi(E, V = 0)$, and the Kramers–Kronig relation yields the real part:

$$\text{Re}[\chi(E)] = -\frac{1}{\pi} \text{Pr} \int_{-\infty}^{+\infty} dE' \frac{\text{Im}[\chi(E')]}{E - E'}$$ (15)

where Pr denotes the Cauchy principal value.

The NRG method divides the entire energy range into discrete sectors of the logarithmic scale, and integrates the high-energy sectors iteratively until the required low-energy sector is reached. In this iterative procedure, it is important to keep the same level of accuracy for the higher-energy sectors (earlier stage of the iteration) because we are interested in the high- energy regime ($E \approx \varepsilon_d, U$) as well as the low-energy range ($|E| < k_B T_K$). To achieve this goal, we adopt the density-matrix NRG method[29,30], where the dynamical excitation spectral density is obtained from the reduced density matrix of each energy sector. In order to enhance the speed and efficiency in the sampling of the spectral peaks in the logarithmic energy scale, we have also used the so-called z-trick[31]. Typically we take the z-average over 32 different z values. In this NRG study, we have found two interesting high-energy properties that have been largely overlooked in previous studies (which mostly have focused on low-energy properties): (i) The charging peak at $E \approx \varepsilon_d$ of the compressibility is shifted from that of the conductance by an amount comparable to Γ. This shift is clearly observable in the experimental result. (ii) The width of the charging peak (at $E \approx \varepsilon_d$) of the conductance for $U \gg \Gamma$ is almost twice as wide as that ($\sim\Gamma$) for the non-interacting case ($U=0$)[32]. This is also consistent with the value of Γ when estimated from the experimentally measured dI/dV data.

Data availability. The main data supporting the findings of this study are available within the article (main text, Methods and Extended Data). Extra data are available from the corresponding author upon request.

26. Wilson, K. G. The renormalization group: critical phenomena and the Kondo problem. *Rev. Mod. Phys.* **47,** 773 (1975).
27. Costi, T. A. & Hewson, A. C. Transport coefficients of the Anderson model. *J. Phys. Condens. Matter* **5,** L361 (1993).
28. Costi, T. A., Hewson, A. C. & Zlatic, V. Transport coefficients of the Anderson model via the numerical renormalization group. *J. Phys. Condens. Matter* **6,** 2519 (1994).
29. Hofstetter, W. Generalized numerical renormalization group for dynamical quantities. *Phys. Rev. Lett.* **85,** 1508 (2000).
30. Weichselbaum, A. & von Delft, J. Sum-rule conserving spectral functions from the numerical renormalization group. *Phys. Rev. Lett.* **99,** 076402 (2007).
31. Yoshida, M., Whitaker, M. A. & Oliveira, L. N. Renormalization-group calculation of excitation properties for impurity models. *Phys. Rev. B* **41,** 9403 (1990).
32. Zitko, R. & Pruschke, T. Energy resolution and discretization artifacts in the numerical renormalization group. *Phys. Rev. B* **79,** 085106 (2009).
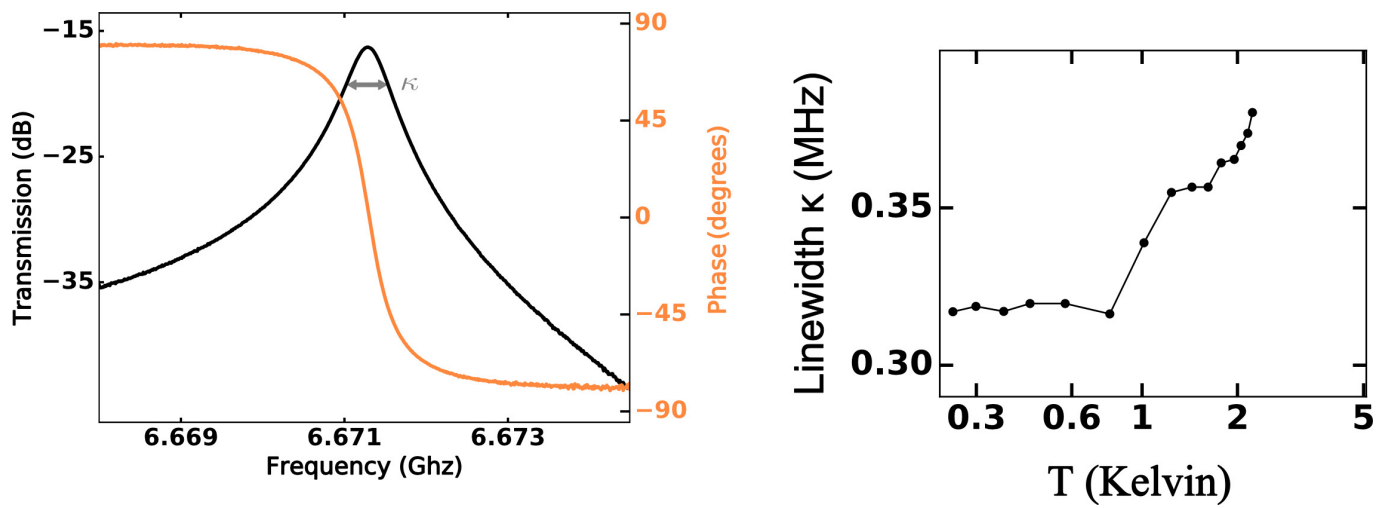
Extended Data Figure 1 | Microwave cavity characterization. Left, phase and amplitude of the microwave signal (plotted as transmission) as a function of frequency showing the cavity resonance used to measure the compressibility. The linewidth of the cavity κ can be read out from this plot as indicated by the grey double arrow. Right, temperature dependence of the linewidth of the cavity, κ.
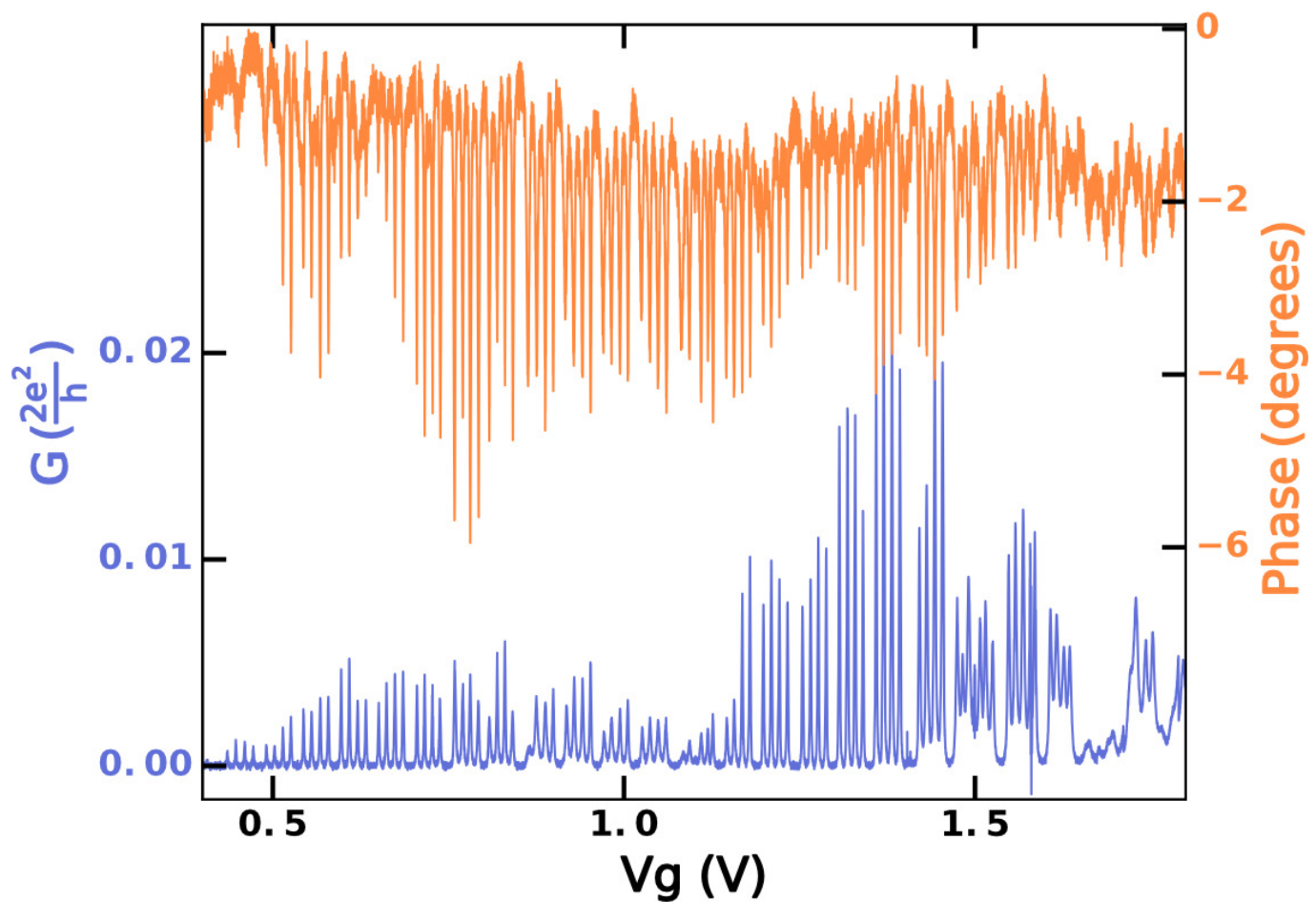
Extended Data Figure 2 | Coulomb blockade regime. Phase and conductance (G) plotted on a wide scale in the Coulomb blockade regime. The observation of groups of four peaks in both the conductance and the phase contrast arises from the spin/valley degeneracy of the nanotube spectrum.
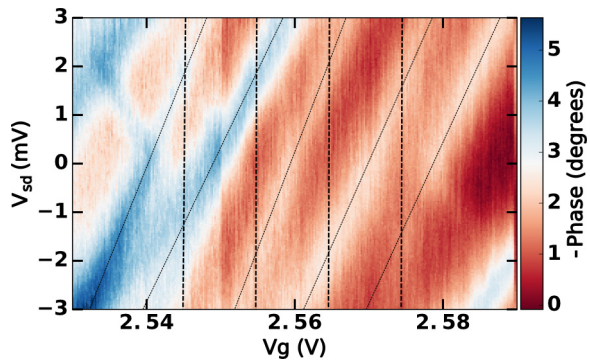
Extended Data Figure 3 | Phase in the Kondo regime. Colour-scale plot of phase in the Kondo regime corresponding to Fig. 3a. We observe tilted lines arising from single charge peaks, but no Kondo ridge. The tilted dotted black lines are guides to the eye. The four vertical dashed lines correspond to the position of the cuts presented in the main text (first, from left to right in this figure), and in the Methods section (third for Extended Data Fig. 7 left panel, and second and fourth for Extended Data Fig. 4). A spurious tilted blue line is also observed. It probably arises from an impurity level coupled to the cavity field.
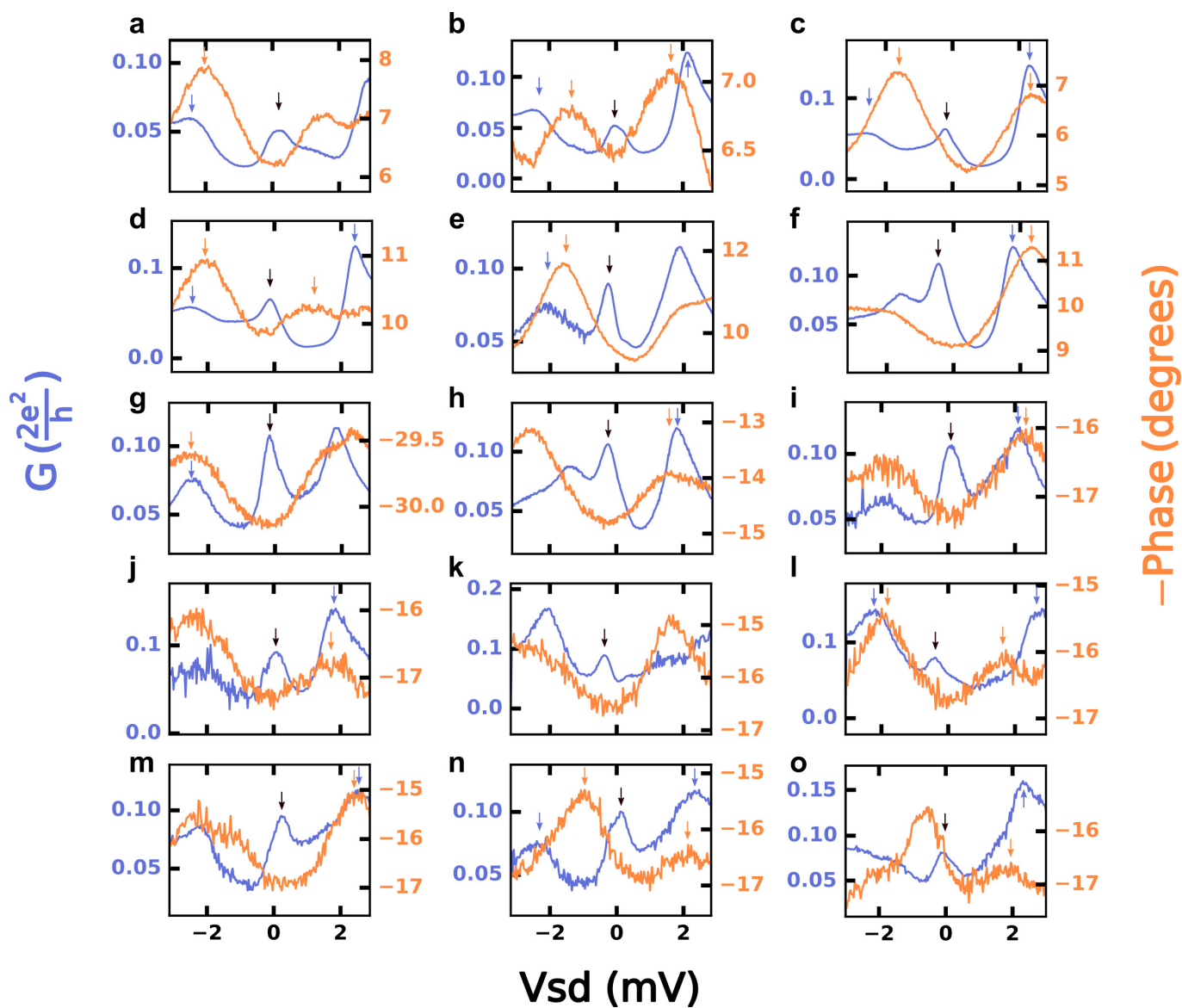
Extended Data Figure 4 | Dual conductance/compressibility measurements for other Kondo ridges. a–o, Examples of 15 different Kondo ridges displaying the same phenomenona as in Fig. 3b. These data correspond to cuts indicated by vertical dashed lines in Extended Data Fig. 5. In particular, the Kondo peak apparent in the conductance (in blue) is always absent from the compressibility (in orange).
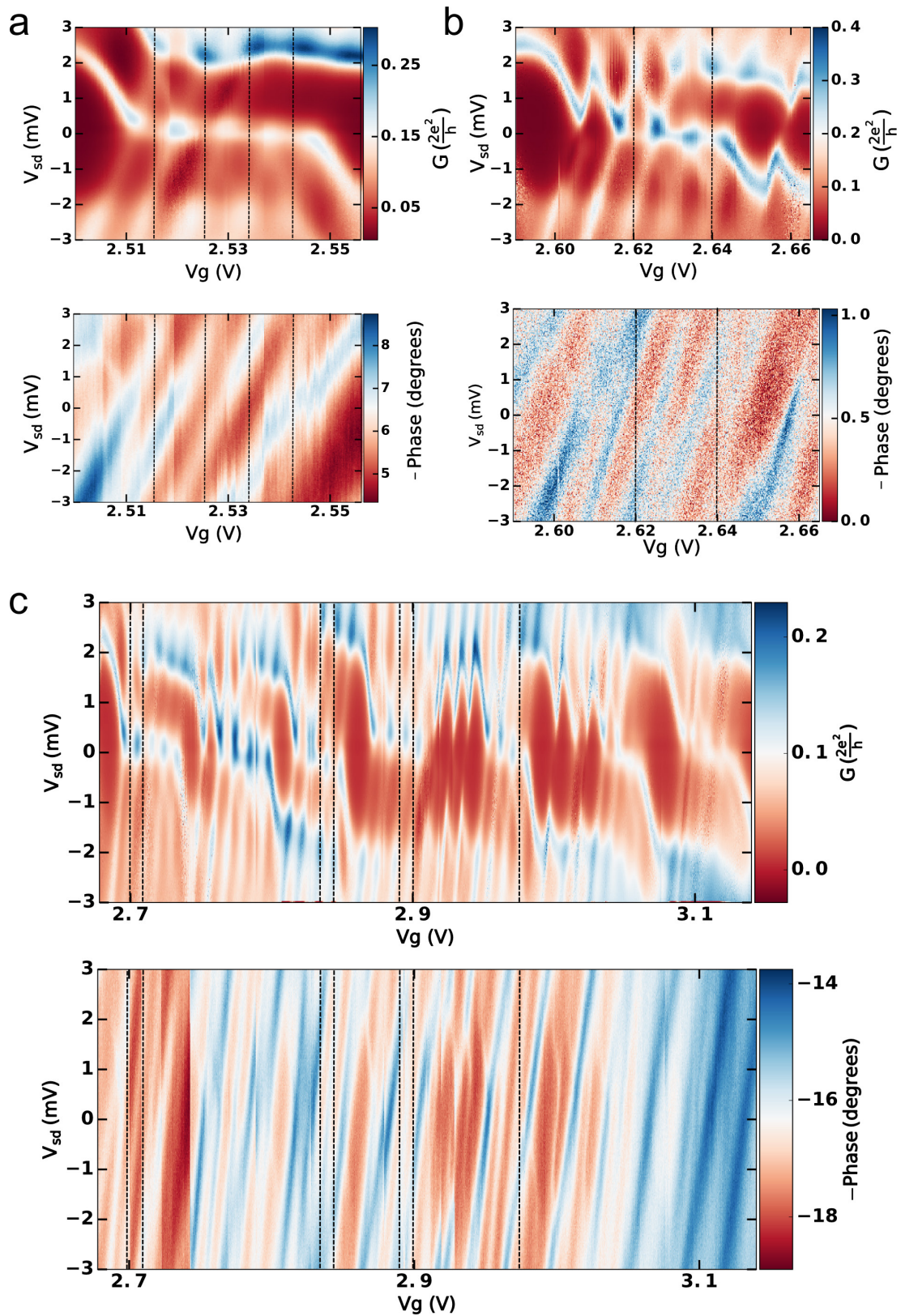
Extended Data Figure 5 | Systematics for the Kondo regime.
a, **b**, Conductance and phase as a function of source–drain bias and gate voltage for Kondo ridges different from the set presented in the main text. **c**, Conductance and phase as a function of source–drain bias and gate voltage on a wide scale in the Kondo regime. The measurements have been performed for a different cool-down (from 2 K to 250 mK) of our ^{3}He single-shot cryostat and correspond to physical parameters different from those for **a** and **b**.
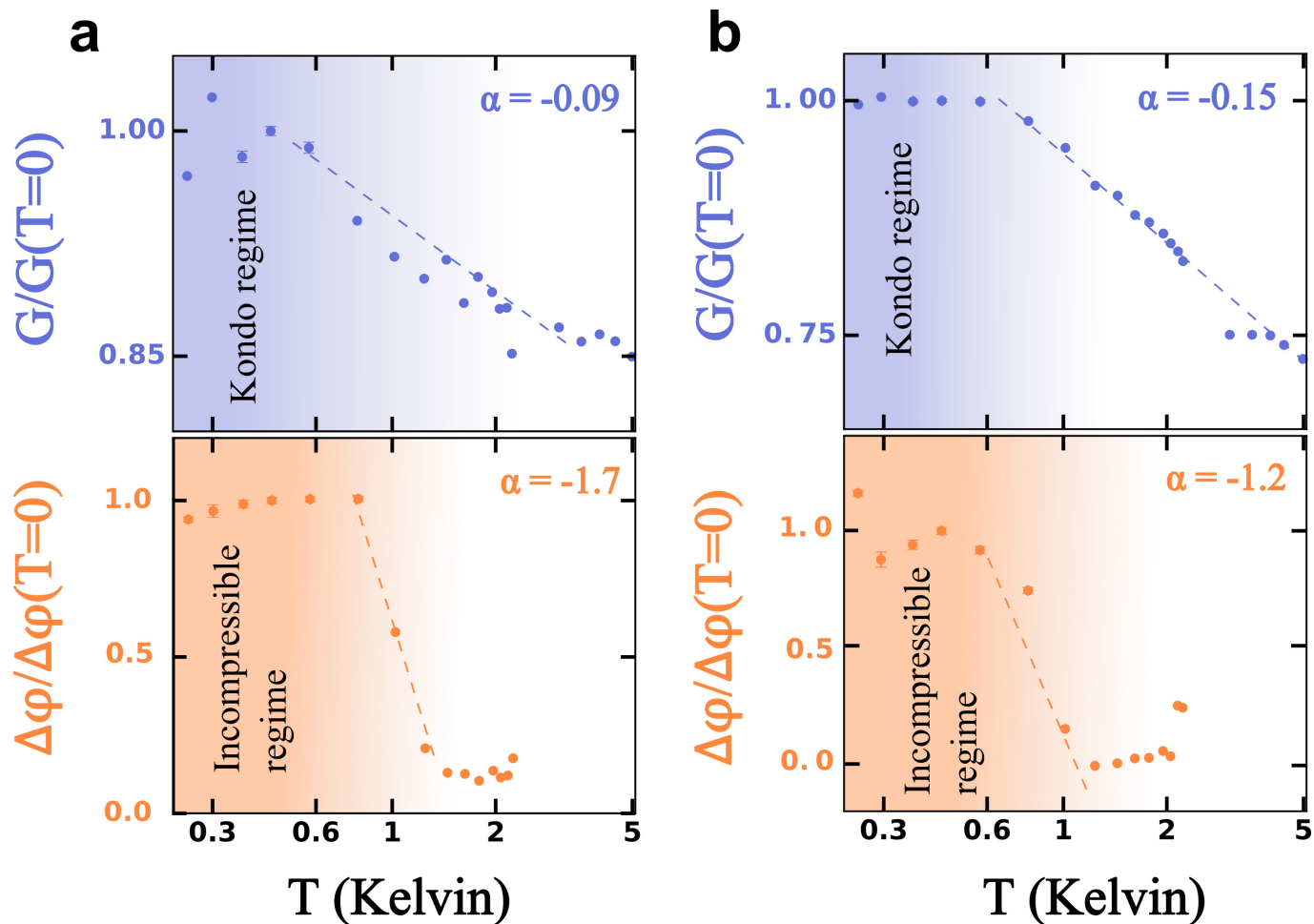
Extended Data Figure 6 | Temperature dependence for other Kondo ridges. a, Conductance (top panel) and phase (bottom panel) as a function of temperature for the second Kondo ridge of Fig. 3a. **b**, As **a** but for the fourth Kondo ridge of Fig. 3a.
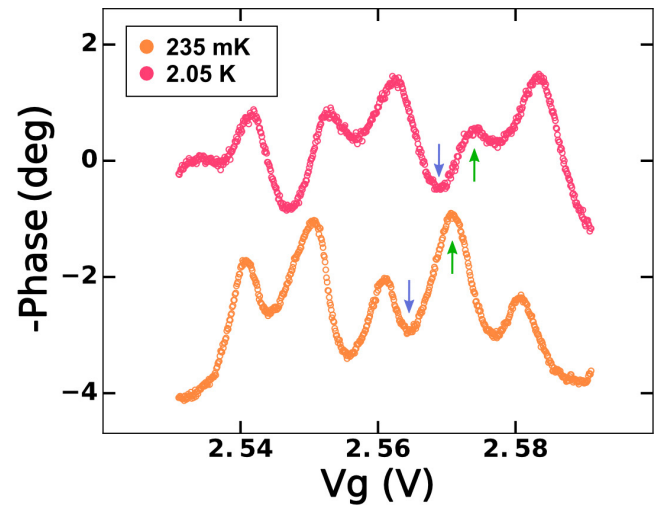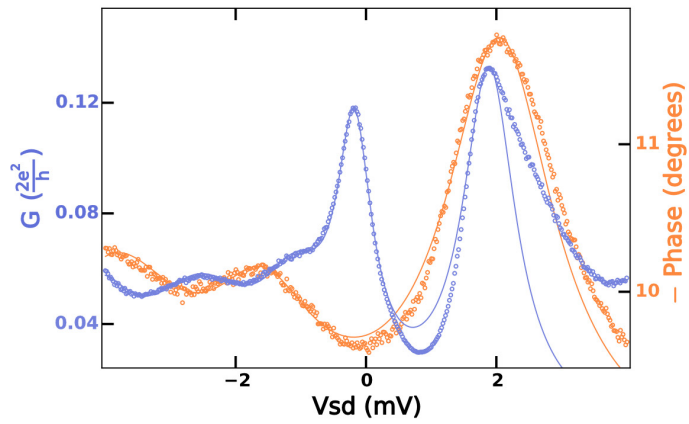
Extended Data Figure 7 | Kondo peak for temperature dependence.
Left panel, bias dependence of conductance and phase for the Kondo ridge used to determine the temperature dependence of Fig. 4a. Right panel, corresponding gate dependence at base temperature (255 mK) and at high temperature (2.05 K). To get rid of the thermal drift of the phase, we compute the difference of the phase between a Coulomb peak (green arrow) and a Coulomb valley (blue arrow), where the Kondo ridge is. The phase at 2.05 K has been rescaled to take into account the decrease of the quality factor of the cavity with temperature (22,000 to 18,000).
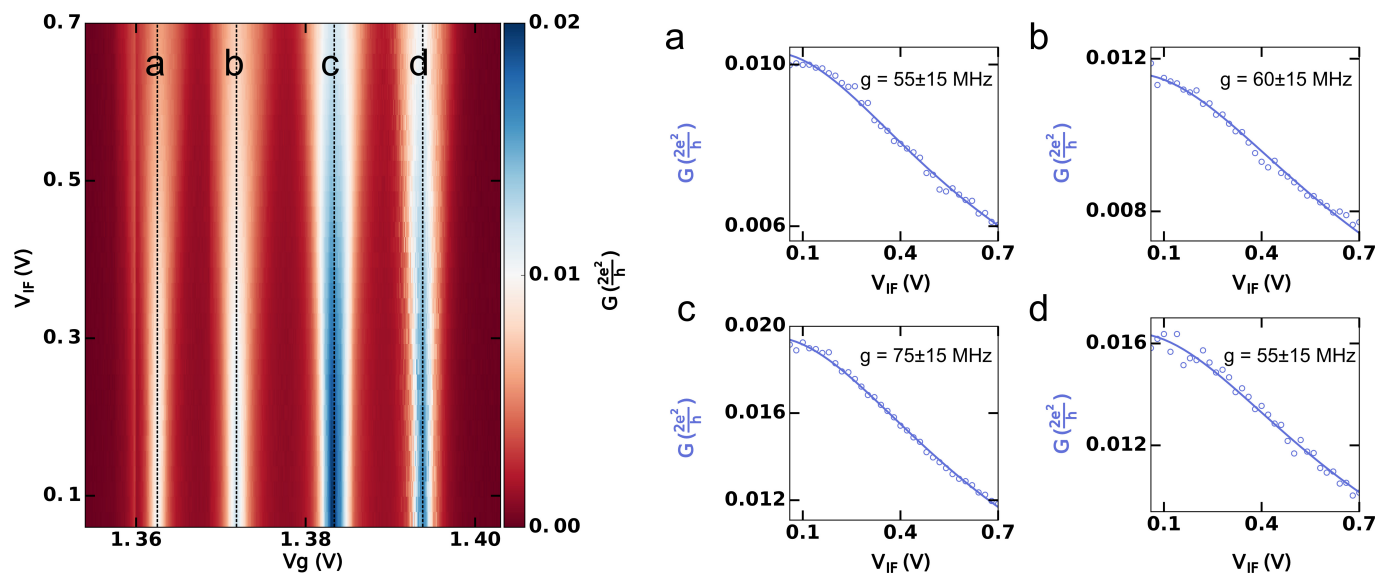
Extended Data Figure 8 | Control experiment for calibration of electron–photon coupling. Power dependence of Coulomb peaks for four different peaks (**a**, **b**, **c** and **d**), shown at left. Each peak height is plotted in the right panels versus the microwave modulation amplitude, which controls the number of photons inside the cavity. The open dots are data and the solid lines are fits using equation (13).